# 3D tomography for multistatic GPR subsurface sensing

Mauricio Pereira[1], Yu Zhang[2], Dan Orfeo[1], Dylan Burns[1], Dryver Huston[1], Tian Xia[1]

[1]School of Engineering, University of Vermont, Burlington, VT 05405, USA
[2]Aptiv PLC, Agoura Hills, CA 91301, USA

## ABSTRACT

Ground penetrating radar (GPR) subsurface sensing is a promising nondestructive evaluation (NDE) technique for inspecting and surveying underground utilities in complex urban environments, as well as for monitoring other key infrastructure such as bridges and railroads. A challenge of such technique lies on image formation from the recorded GPR data. In this work, a fast back projection algorithm (BPA) for three-dimensional GPR image construction is explored. The BPA is a time-domain migration method that has been effectively used in GPR image formation. However, most of the studies in the literature apply a computationally intensive BPA to a two-dimensional dataset under the assumption that an in-plane scattering occurs underneath the GPR antennas. This assumption is not precise for 3D GPR image formation as the GPR radiation scatters in multiple directions as it reaches the ground. In this study, a generalized form for an approximation to determine the scattering point in an air-coupled GPR system is developed which considerably reduces the required computations and can accurately localize the scattering point position. The algorithm is evaluated by applications on GPR data synthesized using GprMax, a finite-difference time domain (FDTD) simulator.

**Keywords**: back-projection algorithm, ground penetrating radar, migration, tomographic reconstruction.

## 1. INTRODUCTION

GPR is a remote NDE sensing technique to detect objects and features underneath the ground surface[1]. In the context of smart cities, GPR surveys are a promising NDE technique for the localization and mapping of underground infrastructure which enables better management, metering and assessment of subterranean infrastructure[2,3]. GPR has also been used for localization of concrete rebars[4], inspection of bridge decks[5,6], and monitoring of railroad ballast[7], etc. Data collected during GPR survey usually requires further processing to avoid incorrect data interpretation, enhance features of interest, or to determine target location and shape[8,9]. A common approach is to apply migration methods to the collected data. Several migration methods are available such as hyperbolic summation (HS)[10], Kirchhoff's migration (KM)[11], phase shift migration (PSM)[12], Stolt migration (SM)[13], and the BPA.

A review of these migration methods applied to GPR 2D B-scan dataset is presented by Ozdemir et al.[14], which evaluates the performances of the methods mentioned above in terms of range and cross-range resolution, integrated sidelobe ratio (ISLR), signal-to-noise ratio (SNR) and computation time. The first three criteria are directly related to the signal focusing ability of each migration method, while the latter is important for practical applications, for instance when real-time (RT) analysis is desired[15]. The results show that the HS and PSM have low focusing ability in comparison to the KM, SM and BPA. These later three approaches are able to spatially determine the targets with good resolution and correct positioning. The KM however is computationally expensive and demands computation time much longer than all other migration algorithms. Hence their study suggests that the two most competitive migration methods are the SM and the BPA. The study[14] concludes that the SM is the best migration method thanks to its lower computation time. However, the SM assumes zero distance between the transmitter and receiver antennas. Such assumption is not applicable for bistatic or mulstistatic radar where the transmitter antenna and receiver antenna are spatially separated. Moreover, the standard SM does not consider layered media, i.e. it assumes that the underground media is homogeneous and the scattered field is sensed at the ground level. To consider a layered media, the standard SM must be modified. One approach is to combine the PSM and SM, using the PSM to determine layers interface and the SM within each layer[16], but that increases the computation time.

The BPA is a time-based migration method that can be used to recover target depth and shape from GPR A-scan data set. The algorithm back-projects the emitted signal based on EM wave travel path and the associated travel time, analogous to the traditional back-projection methods in computer aided tomography[17,18]. The BPA is suitable for imaging subsurface in layered media[19], and thus is suitable for processing data of air-coupled GPR systems in contrast with the SM. Also, the BPA does not require full data collection prior to algorithm computation, hence it can be potentially employed in real time analysis[15] and parallel computation. Therefore, BPA is an attractive migration method for GPR data processing and is adopted in this work. For air-coupled GPR systems, considerable complexity and computational cost are involved to back project the scattering point on the wave travel path in BPA. For instance, if the height of the antennas in relation to the ground is assumed constant, determination of the scattering point yields a fourth order polynomial equation to resolve for the horizontal position[19].

In the 2D case, a simplification introduced by Mast & Johansson[20] can be used to estimate the scattering point with a good accuracy without the need to solve the fourth order polynomial equation. But Zhou, Huang & Su[19] noticed that such approximation is inaccurate if the distance between the antennas and the target is large.

In the 3D case, several other complications are introduced. For instance, the scattered wave pattern is highly dependent on the reflecting surface orientation and roughness. The refracted wave might not be within the same plane of the incident wave, implying that multiple refracting directions must be considered for proper signal back-projection. In that scenario, the number of calculations required becomes too large, rendering the BPA impractical.

One approach to circumvent these limitations is to consider the signals only in the direction of antennas main emission, thus capturing those signals with higher SNR while greatly reducing the number of points computed. This requires the knowledge of antenna radiation pattern and information about radar orientation for each A-scan. We suggest another approach using the assumption that the refracted wave will remain in the same plane of the incident wave, i.e., that most of the energy will be scattered in the same plane as the incident wave, such that only this plane can be considered for back-projection. Under such assumption, we are able to extend the approximation methods given by Zhou, Huang & Su[19] and Mast & Johansoon[20] by applying the appropriate change of coordinates, rendering a 3D back-projection algorithm that has a lower computational cost in comparison to a full 3D back-projection. We develop this approach and apply the algorithm to the synthetic data generated with GprMax[21].

This paper is organized as follows: In section 2 both the 2D and 3D approximation for the scattering point location are introduced, as well as the 3D BPA. In section 3 the BPA results for synthesized data are presented and discussed. Finally, in section 4 the concluding remarks are given.

## 2. METHODOLOGY

### 2.1. 2D scattering point approximation

The refraction of the GPR signal in a bistatic air-coupled GPR system is illustrated in Fig. 1a. To determine the horizontal position $x_S$ of the scattering point, a fourth-order polynomial must be resolved, which is computationally intensive, especially considering that this equation needs to be resolved iteratively for each transmitter and receiver position to cover all observation angles. To reduce the computation, an approximation method is adopted[19] . Assuming a homogeneous media, the horizontal position of the scattering point is then given by

$$x_S = \begin{cases} x_P + \dfrac{x_c - x_p}{\sqrt{\epsilon_r}}, & |x_T - x_P| < (z_P + h)\sqrt{\epsilon_r/(\epsilon_r - 1)} \\ x_p + \dfrac{z_P}{\sqrt{\epsilon_r - 1}}, & x_T \geq x_P + (z_P + h)\sqrt{\epsilon_r/(\epsilon_r - 1)} \\ x_p - \dfrac{z_P}{\sqrt{\epsilon_r - 1}}, & x_T \leq x_p - (z_P + h)\sqrt{\epsilon_r/(\epsilon_r - 1)} \end{cases}, \quad (1)$$

where $x_p$ is the horizontal position of the point of interest, $z_p$ is the depth of the point of interest, $x_T$ is the transmitter horizontal position, $h$ is the transmitter height assumed to be constant, $x_c$ is the point where a straight line connecting $x_p$ and $x_T$ intersects the ground, and $\epsilon_r$ is the ground relative dielectric constant. For ground-coupled GPR systems, the back-projection is simpler as the wave travel path is assumed to be a straight line, as shown in Fig. 1b. The first case in equation (1) above corresponds to the approximation previously introduced by Mast & Johansson[20].

Notice that the approximation (1) can also be used to determine the scattering point horizontal position $\tilde{x}_S$ from the point P to the receiver (see Fig.1a) by considering the point P as a source, analogous to the exploding source model[22]. In the following discussion the development is made in terms of the transmitter point of view, but these approximations are also used to determine the wave path back to the receiver.

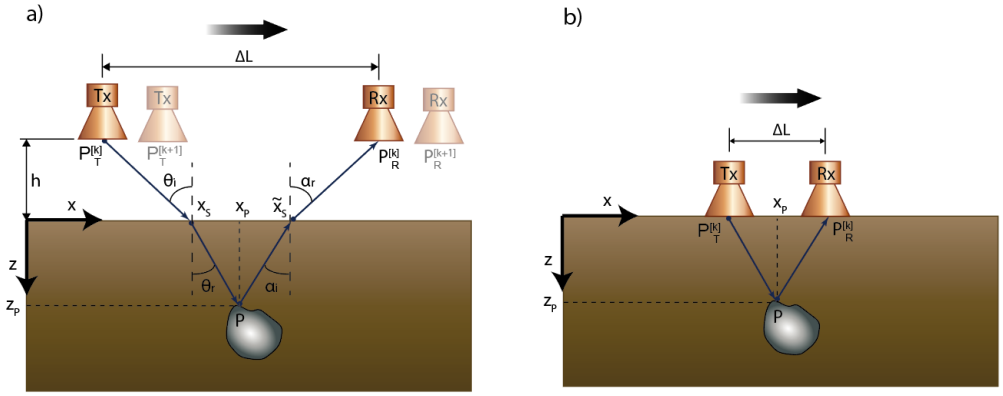


Figure 1: Diagram of the wave path considering a bistatic pair in (a) air-coupled GPR system and (b) ground-coupled GPR system.

### 2.2. 3D scattering point approximation

Consider now the general air-coupled 3D case illustrated in Fig. 2. Assume that the transmitter antenna behaves like a point source emitting spherical electromagnetic waves. Once the wave reaches the ground, both refraction and reflection occur. Depending on ground geometry and texture, the refracted wave can be very complex and hard to model. If all possible refracted directions are considered, computational cost increases tremendously, as such consideration must be applied to all scattering points. To enable the usage of the BPA, some simplifying assumptions are made to reduce the computational cost.

Assume that the ground surface is planar, the transmitter is perpendicular to such surface, and the ground is homogeneous with a dielectric constant $\epsilon_r$. The key assumption in our algorithm is that the main refraction remains in the same plane as the emitted wave, i.e., the path $P_T^{[k]} \rightarrow A$ is in the same plane as the path $A \rightarrow P$ in Fig. 2a.

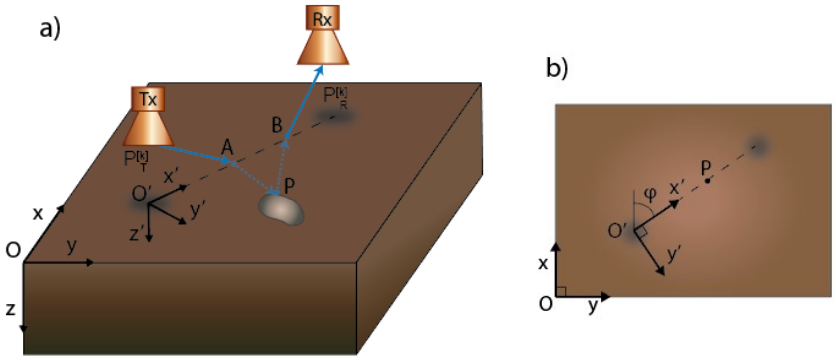


Figure 2: A 3D diagram of a bistatic pair, (a) illustrates the wave path in the $x'z'$ plane and (b) the corresponding bird's eye view.

In a general 3D domain, a homogeneous transformation[23] is used to express Eq. (1) for any plane perpendicular to the ground. A homogeneous transformation expresses both a rotation and a translation using a 4x4 matrix, and to operate with it an extra unitary coordinate is added to the point coordinate to account for the translation. Consider the bird's eye view depicted in Fig. 2b. Let $Oxyz$ be a fixed frame of reference and $O'x'y'z'$ a rotating frame of reference at the same position as the transmitter but on ground level, such that $x'$ points to the wave horizontal propagation direction. The coordinates of a point P expressed in the $O'x'y'z'$ reference frame can be transformed to $Oxyz$ coordinates using the homogeneous transformation

$$\boldsymbol{p} = \boldsymbol{H}\boldsymbol{p}', \tag{2}$$

where $\boldsymbol{p}$ is the homogeneous representation of point $P$ in the $Oxyz$ reference frame, $\boldsymbol{p}'$ the homogeneous representation of P in the $O'x'y'z'$ reference frame, and $\boldsymbol{H}$ is the transformation matrix given by

$$\boldsymbol{H} = \begin{bmatrix} \cos(\phi) & -\sin(\phi) & 0 & x_T \\ \sin(\phi) & \cos(\phi) & 0 & y_T \\ 0 & 0 & 1 & 0 \\ 0 & 0 & 0 & 1 \end{bmatrix}, \tag{3}$$

where $\phi$ is the angle between $x$ and $x'$ as shown in Fig. 2b.

Let $P$ be a point that lies on the $x'z'$ plane as shown in Fig 2b. Then $\boldsymbol{p}' = [x', 0, z', 1]^T$. Expanding the transformation (2) yields the following set of equations

$$x = \cos(\phi)\, x' + x_T, \tag{4}$$
$$y = \sin(\phi)\, x' + y_T, \tag{5}$$
$$z = z'. \tag{6}$$

Notice that the $z$ coordinate is unaltered by this transformation. Isolating $x'$ in the expressions above, it has

$$x' = \frac{x - x_T}{\cos(\phi)}, \tag{7}$$
$$x' = \frac{y - y_T}{\sin(\phi)}. \tag{8}$$

Consider the squared Snell's law applied to the $x'y'$ plane

$$\sin(\theta_i)^2 = \epsilon_r \sin(\theta_r)^2, \tag{9}$$

with $\theta_i$ and $\theta_r$ as illustrated in Fig. 1a and $\epsilon_r$ being the dielectric constant of the ground. As $|x_T - x_S| \rightarrow \infty$, the incident angle tends to equal 90° and $\sin(\theta_i) \rightarrow 1$. Thus, for a transmitter distant from the point of interest, equation (6) yields

$$z_P'^2 + (x_P' - x_S')^2 = \epsilon_R (x_P' - x_S')^2. \tag{10}$$

Isolating $x_S'$

$$x_S' = x_P' - \frac{z_P'}{\sqrt{\epsilon_r - 1}}, \tag{11}$$

where we assume, without loss of generality, that $x_P > x_S > x_T$.

Substituting Eq. (7) into Eq. (10) and isolating $x_S$ leads to

$$x_S = x_P - \frac{z_P \cos(\phi)}{\sqrt{\epsilon_r - 1}}. \tag{12}$$

Notice that the sign of $\cos(\phi)$ accounts for the cases where $x_T > x_P$.
We also have from the approximation[20]

$$x'_S = x'_P + \frac{(x'_C - x'_P)}{\sqrt{\epsilon}_r}, \tag{13}$$

where $x'_C$ is the point at which the line connecting $x'_T$ and $x'_P$ intersects the ground line, given by

$$x'_C = x'_T + \frac{x'_P - x'_T}{z'_P + h} h. \tag{14}$$

Applying Eq. (7) on Eq. (13) and Eq. (14) gives, respectively

$$x_S = \frac{\sqrt{\epsilon_r} - 1}{\sqrt{\epsilon_r}} x_P + \frac{x_C}{\sqrt{\epsilon_r}}, \tag{15}$$

$$x_C = x_T + \frac{x_P - x_T}{z_P + h} h. \tag{16}$$

Then substituting Eq. (16) into Eq. (15) we have

$$x_S = x_P + \frac{z_P (x_T - x_P)}{\sqrt{\epsilon_r}(z_P + h)}. \tag{17}$$

Eq. (12) is a better approximation for scene points that are away from the transmitter while Eq. (17) is a better approximation for scene points close to the transmitter. To establish a choice criterion, we look for the point where Eq. (12) and Eq. (17) yield the same scattering point. Imposing this equality condition leads to

$$x_P - x_T = \cos(\phi) \frac{(z_P + h)\sqrt{\epsilon_r}}{\sqrt{\epsilon_r - 1}}. \tag{18}$$

Therefore, we propose the following approximation for the scattering point $x_S$ of an 3D air-coupled GPR system

$$x_S = \begin{cases} x_P + \dfrac{z_P (x_T - x_P)}{\sqrt{\epsilon_r}(z_P + h)}, & if\ |x_P - x_T| \le |\cos(\phi)| \dfrac{(z_P + h)\sqrt{\epsilon}}{\sqrt{\epsilon_r - 1}} \\ x_P - \dfrac{z_P \cos(\phi)}{\sqrt{\epsilon_r - 1}}, & if\ |x_P - x_T| > |\cos(\phi)| \dfrac{(z_P + h)\sqrt{\epsilon}}{\sqrt{\epsilon_r - 1}} \end{cases} \tag{19}$$

where

$$\cos(\phi) = \frac{x_P - x_T}{\sqrt{(x_P - x_T)^2 + (y_P - y_T)^2}}. \tag{20}$$

Then Eq. (7) combined with Eq. (8) is used to obtain the corresponding y-axis position for a given $x$ as

$$y = y_T + \frac{y_P - y_T}{x_P - x_T}(x - x_T). \tag{21}$$

### 2.3. Back-projection algorithm

Initially we develop the BPA for a bistatic pair. Extension to multistatic GPR systems with an arbitrary number of transmitters and receivers can be readily obtained by extending the bistatic case and is presented in sequence.

#### 2.3.1. BPA for bistatic GPR image formation

Consider the air-coupled bistatic pair taking the k[th] A-scan illustrated in Fig. 2a. The transmitter is at position $P_T^{[k]} = \left(x_T^{[k]},\ y_T^{[k]},\ -h\right)$ and the receiver at position $P_R^{[k]} = \left(x_R^{[k]},\ y_R^{[k]},\ -h\right)$. For the ground-coupled GPR scan, the signal travel path is assumed to be a line from the transmitter to the point of interest in the domain. Thus, it is not necessary to introduce a homogeneous transformation as the wave path can be readily calculate as the Euclidean distance between the transmitter position and the point of interest. In this study, our focus is on BPA image formation for the air-coupled GPR scan.

Assume that the distance between transmitter and receiver is fixed. The positions of the bistatic pair, instead of each transmitter and receiver individual positions, are enumerated. Then for the bistatic pair being is at the position k, it asserts that transmitter and receiver are at positions $P_T^{[k]}$ and $P_R^{[k]}$, respectively. The signal collected by the bistatic pair receiver at position $k$ at time instant t is $s^{[k]}(t)$. In practice, the signal is sampled at a finite number of points, to increase the resolution, interpolations are performed in the algorithm implementation.

The position of the scattering points A and B shown in Fig. 2a are given by $(x_A^{[k]},\ y_A^{[k]},\ 0)$ and $\left(x_B^{[k]},\ y_B^{[k]},\ 0\right)$, respectively, and are calculated using the expressions given in Eq. (19) and Eq. (21) as a function of $P_T^{[k]},\ P_R^{[k]}$, and a given point P in the domain.

The round-trip time from an air-coupled transmitter to a point $P$ of interest in the domain and back to the receiver is given by

$$t\left(P, P_T^{[k]}, P_R^{[k]}\right) = \left(\frac{d_{TA}^{[k]}}{c} + \frac{d_{AP}^{[k]}}{v}\right) + \left(\frac{d_{PB}^{[k]}}{v} + \frac{d_{BR}^{[k]}}{c}\right), \tag{22}$$

where the first term on the right-hand side of the equation represents the wave travel time from the transmitter to the point of interest, and the second term represents the wave travel time from the point of interest back to the receiver as shown in Fig. 2a.

For the ground-coupled GPR system

$$t\left(P, P_T^{[k]}, P_R^{[k]}\right) = \frac{d_{TP}^{[k]} + d_{PR}^{[k]}}{v}. \tag{23}$$

In both Eq. (22) and Eq. (23), $c$ is the speed of light, and $v = c/\sqrt{\epsilon_r}$ is the speed of the wave in the subsurface medium. Let $d_{AB}^{[k]}$ denote the distance from a generic point A to a generic point B in the k-th scan. Then the distances in Eq. (22) are expressed as

$$d_{TA}^{[k]} = \sqrt{\left(x_A^{[k]} - x_T^{[k]}\right)^2 + \left(y_A^{[k]} - y_T^{[k]}\right)^2 + h^2}, \tag{24}$$

$$d_{AP}^{[k]} = \sqrt{\left(x_P - x_A^{[k]}\right)^2 + \left(y_P - y_A^{[k]}\right)^2 + z_P^2}, \tag{25}$$

$$d_{PB}^{[k]} = \sqrt{\left(x_P - x_B^{[k]}\right)^2 + \left(y_P - y_B^{[k]}\right)^2 + z_P^2}, \tag{26}$$

$$d_{BR}^{[k]} = \sqrt{\left(x_B^{[k]} - x_R^{[k]}\right)^2 + \left(y_B^{[k]} - y_R^{[k]}\right)^2 + h^2}, \tag{27}$$

and in Eq. (23) as

$$d_{TP}^{[k]} = \sqrt{\left(x_T^{[k]} - x_P\right)^2 + \left(y_T^{[k]} - y_P\right)^2 + z_P^2}, \tag{28}$$

$$d_{PR}^{[k]} = \sqrt{\left(x_R^{[k]} - x_P\right)^2 + \left(y_R^{[k]} - y_P\right)^2 + z_P^2}. \tag{29}$$

To implement the BPA algorithm, a set of points of interest in the domain are selected. Consider for instance a spatial regular grid given by $[x_1, \dots, x_{N_x}] \times [y_1, \dots, y_{N_y}] \times [z_1, \dots, z_{N_z}]$. For each position $k$ of the bistatic pair the travel times of all domain points are calculated using Eq. (22) for an air-coupled GPR system or Eq. (23) for a ground-coupled GPR system. The calculated times can be stored in an array. The points in the domain are enumerated to calculate the coordinates of each point $P_i$, where $i = 1 \dots N$, and $N = N_x \times N_y \times N_z$. Then, in the case where $M$ A-scans are taken, the round-trip times are stored in an array as

$$T = [t_{i,k}], \qquad i = 1 \dots N, \qquad k = 1 \dots M, \tag{30}$$

where

$$t_{i,k} = t\left(P_i, P_T^{[k]}, P_R^{[k]}\right). \tag{31}$$

The array in Eq. (30) records the travel times from a bistatic pair at position k to all points $P_i$. An advantage of calculating Eq. (30) is that it can be highly parallelized to reduce the computation time. Since the points in the domain are enumerated, this representation facilitates the algorithm implementation. Furthermore, considering a given bistatic pair at position $k$ and a given point $P_i$, the corresponding received signal is

$$s_{i,k} = s^{[k]}(t_{i,k}). \tag{32}$$

The domain can be represented as a tridimensional matrix $D_{N_x \times N_y \times N_z}$ where each component holds the added signals. For a point $P_i$ we have the corresponding coordinates $(x_l, y_m, z_l)$ and the associated index $(l, m, n)$ in $D$, such that the signal $s_{i,k}$ can be added to $D(l, m, n)$. Let the addition of the signal $s_{i,k}$ to the appropriate index of the point $P_i$ be represented as $s_{i,k}|_{P_i}$, then the full application of BPA is expressed as

$$D = \sum_{k=1}^{M} \sum_{i=1}^{N} s_{i,k}|_{P_i}. \tag{33}$$

Eq. (33) highlights using an array in Eq. (30) is convenient for implementation, as we can use lookup tables for the appropriate position indexes while retain a simple description of the algorithm. For a survey performed in an irregular grid, scan positions can be stored as an array of coordinates for the corresponding A-trace. Furthermore, Eq. (30) shows that the BPA image is formed by adding signals of all collected A-scans to the appropriate locations in the domain.

### 2.3.2. BPA for multistatic GPR image formation

Consider a multistatic GPR system composed of P transmitters and Q receivers. The image formed by the q$^{th}$ receiver can be computed using Eq. (33) for each transmitted signal and summing each resulting image. Then the image formed by the q$^{th}$ receiver $D^q$ is

$$D^q = \sum_{p=1}^{P}\sum_{k=1}^{M}\sum_{i=1}^{N} s_{i,k}^{p,q}|_{P_i}, \tag{34}$$

with

$$s_{i,k}^{p,q} = s^{[p,q,k]}\left(t_{i,k}^{p,q}\right), \tag{35}$$

$$t_{i,k}^{p,q} = t\left(P_i, P_p^{[k]}, P_q^{[k]}\right), \tag{36}$$

where $s^{[p,q,k]}(t)$ denotes the signal emitted by the p[th] transmitter collected by the q[th] receiver with the GPR system at the k[th] position at a time $t$, and $t_{i,k}^{p,q}$ now uses Eq. (31) with the corresponding position $P_p^{[k]}$ of the p[th] transmitter and $P_q^{[k]}$ of the q[th] receiver. Furthermore, $s_{i,k}^{p,q}|_{P_i}$ denotes the addition of the signal collected by the q[th] receiver from the p[th] transmitter at time $t_{i,k}^{p,q}$ when the GPR system is at position k to the appropriate domain point $P_i$. To compose the final image, all the images formed by each receiver are added. Thus, for a multistatic GPR system the full application of the BPA is

$$D = \sum_{q=1}^{Q} D^q = \sum_{p=1}^{P}\sum_{q=1}^{Q}\sum_{k=1}^{M}\sum_{i=1}^{N} s_{i,k}^{p,q}|_{P_i}. \tag{37}$$

Notice that the application of the BPA implies that points of a real target will get signal contributions from many receivers. For instance, consider Fig. 3. Each spherical surface represents signal contributions from different radar positions. As these signals are added to form the BPA image, a real target position will be at the intersection of the contributing signals, illustrated by the dark point in Fig. 3. This leads to the focusing of the signal at that point and potential recovery of object's shape.

However, in the algorithm implementation a discretized domain must be used, and the set of points might not exactly coincide with the intersecting points. To account for that, interpolation of the sampled signal is required. A way to circumvent this limitation is by increasing the number of points around a region of interest.

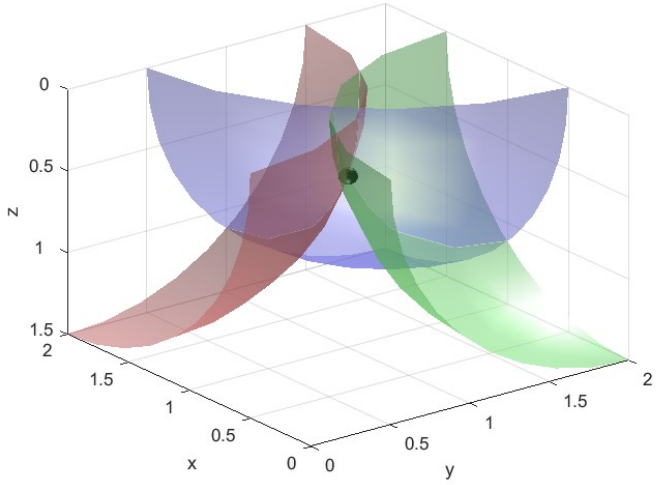


Figure 3: Scheme of the signal focusing using BPA. Each spherical surface represents signal contribution from different radar positions. All signals contribute to the intersecting point, such that the accumulated value is higher at the real target location.

The algorithm steps can be summarized as follows:

1. Define a set of points of interest in the domain.
2. Calculate the travel times from each point in the domain to each position of the antennas using equation (22). This step can be computed in parallel.
3. For each receiver antenna in the domain, using the times calculated in step 2, retrieve signal value and add contributions to the domain points. This step requires signal interpolation since the collected signal is discrete. Addition to points can be performed in parallel, but for one antenna at each time.

## 3. RESULTS

In our implementation, we take advantage of the lower number of computations under the same plane refraction assumption and the high parallelization potential of Eq. (30) and Eq. (33) to reduce computation time. We use CUDA for GPGPU on a standard commercial notebook to dramatically reduce computation time. In the following discussion, dimensions are given as width versus length versus height or depth.

### 3.1. Synthetic GPR data

To synthesize 3D GPR data, the FDTD based GPR simulator GprMax is used. Two models are considered, including, a block buried in concrete, and crossed cylinders in a concrete slab. In all simulations, the dielectric constants are set as $\epsilon_{concrete} = 6$ and $\epsilon_{target} = 8$. Furthermore, a radar system moves in x direction in each B-scan as illustrated in Fig. 3.

In the bistatic case (Fig. 3a), the receiver is positioned ahead of the transmitter and they are aligned with the scan direction. Details about the distances are given for each experiment. In the mulstitatic arrangement (Fig. 3b), two extra receivers are added to the bistatic configuration. They are positioned parallel to the central receiver perpendicular to the scan direction.

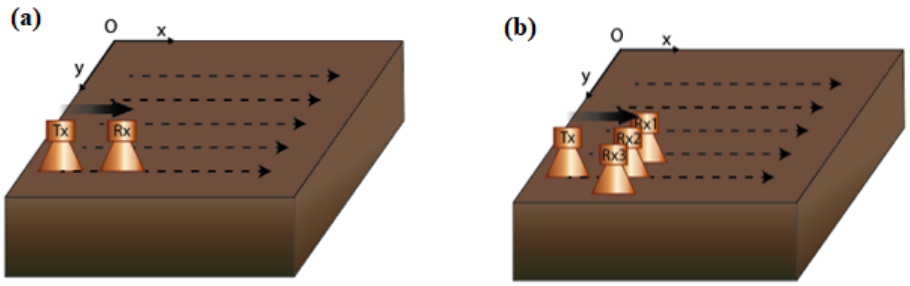


Figure 4: B-scans are performed along the x-axis by (a) bistatic radar, except for the last simulation where a (b) multistatic radar is used. Several B-scans are taken to compose a C-scan that is used as the input for the BPA.

### 3.1.1 Block buried in concrete

A model of a block of dimensions 100x100x50 mm buried at a depth of 50 mm inside a concrete slab is considered as a sample target. An air-coupled GPR simulation, with the bistatic pair at a height of 100 mm above the ground is performed (Fig. 4a). The transmitter antenna is a Hertzian dipole antenna, and the radiation signal is a second order Ricker wave with center frequency of 2 GHz. The synthesized B-scan consists of 40 A-scans, 10 mm apart of each other. The receiver is 50 mm away from the transmitter in the scanning direction. To compose the C-scan, 17 B-scans were created, each apart by 20 mm in the y direction. A domain of dimensions 300x300x150 mm is discretized in 50x50x50 elements for the execution of the BPA. The resulting BPA image is shown in Fig. 5. The top figure shows a 3D view of the result with isosurfaces highlighting the top and bottom surfaces of the buried block. Figures (5b) and (5c) show the indicated cross sections of the BPA image, while figures (5d) and (5e) show the corresponding input data for these cross sections. The BPA is able to form the bottom and top faces of the block indicating that Eq. (19) works well for the considered range.

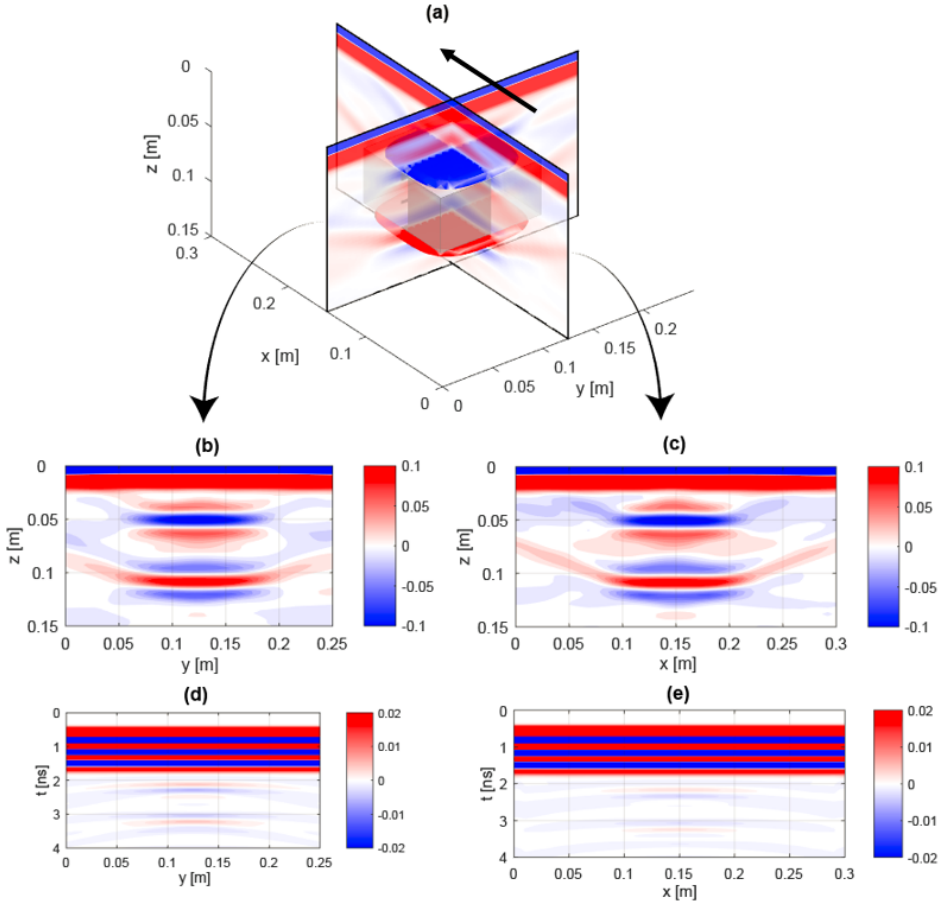


Figure 5: Resulting image of BPA applied on a synthetic bistatic air-coupled C-scan of a block buried in concrete. (a) 3D view, arrow indicates GPR B-scan direction; (b) and (c) shows the indicated cross sections; (d) and (e) shows the corresponding raw data of each cross section.

### 3.1.2. Crossed cylinders in concrete

In the second simulation, crossed cylinders in a concrete slab are considered. The first cylinder, whose longitudinal axis is parallel to the y-axis, has a diameter of 25.4 mm and is at a depth of 64 mm. The second, transversal cylinder has a diameter of 25.4 mm, and is buried at a depth of 88 mm. An air-coupled GPR simulation is performed with the bistatic pair at a height of 100 mm above the ground (Fig. 4a). The transmitter antenna is an ideal Hertzian dipole emitting second order Ricker waves with center frequency of 2 GHz that was used to generate B-scans, each composed of 40 A-scans 10 mm apart of each other. To compose the C-scan, 21 B-scans are generated, each apart by 10 mm. The synthetic data is time-gated to remove the ground reflection. The domain dimension is 200x400x150 mm and is discretized with 40x20x40 elements. The resulting image is shown in Fig. 6. The top figure shows a 3D view of the result with isosurfaces highlighting the bottom surfaces of the cylinders. Figures (6b) and (6c) show the indicated cross sections of the BPA image, while figures (6d) and (6e) show the corresponding input data for these cross sections. The position and arrangement of the cylinders are recovered, but it is harder to recover isosurfaces that isolate exclusively the cylinders position. The shape is also not recovered due to the wavelength resolution.

Furthermore, the same setup is scanned with a multistatic air-coupled GPR system with one transmitter and three parallel receivers as illustrated in Fig 4b. The receivers are 50 mm in front of the transmitter and 50 mm apart from each other. The domain is discretized to a grid of 40x20x40. The raw data is time gated to remove the ground reflection. The resulting BPA image is show in Fig. 7. The top figure shows a 3D view of the result with isosurfaces highlighting the bottom surfaces of the cylinders. Figures (7b) and (7c) show the indicated cross sections of the BPA image, while figures (7d) and (7e) show the corresponding input data for these cross sections. Notice that results vary slightly in relation to the bistatic case, suggesting that the middle antenna dominates over other signals. In the air-coupled system, the signal loss is higher, so stronger signals can dominate the image. For instance, in Fig. 7c, notice the circular-like shape around the top cylinder. Because the signal close to the cylinder is significantly higher than in other positions, this signal contribution is noticeable throughout the domain. Nonetheless, the resulting composition of signals given by the BPA is still focused at the cylinder position and can be clearly distinguished.

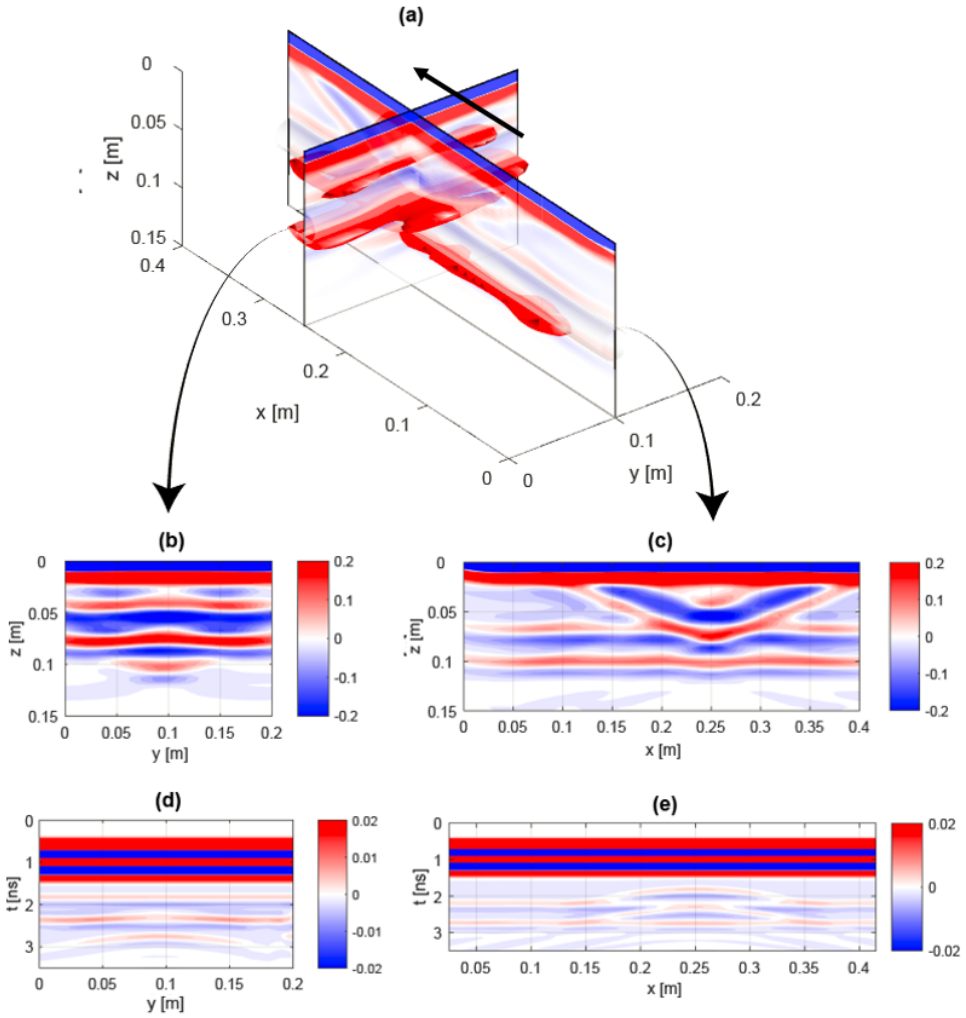


Figure 6: Resulting image of BPA applied on a synthetic bistatic air-coupled C-scan of a concrete slab with two crossing cylinders. (a) 3D view, arrow indicates GPR B-scan direction; (b) and (c) shows the indicated cross sections; (d) and (e) shows the corresponding raw data of each cross section.

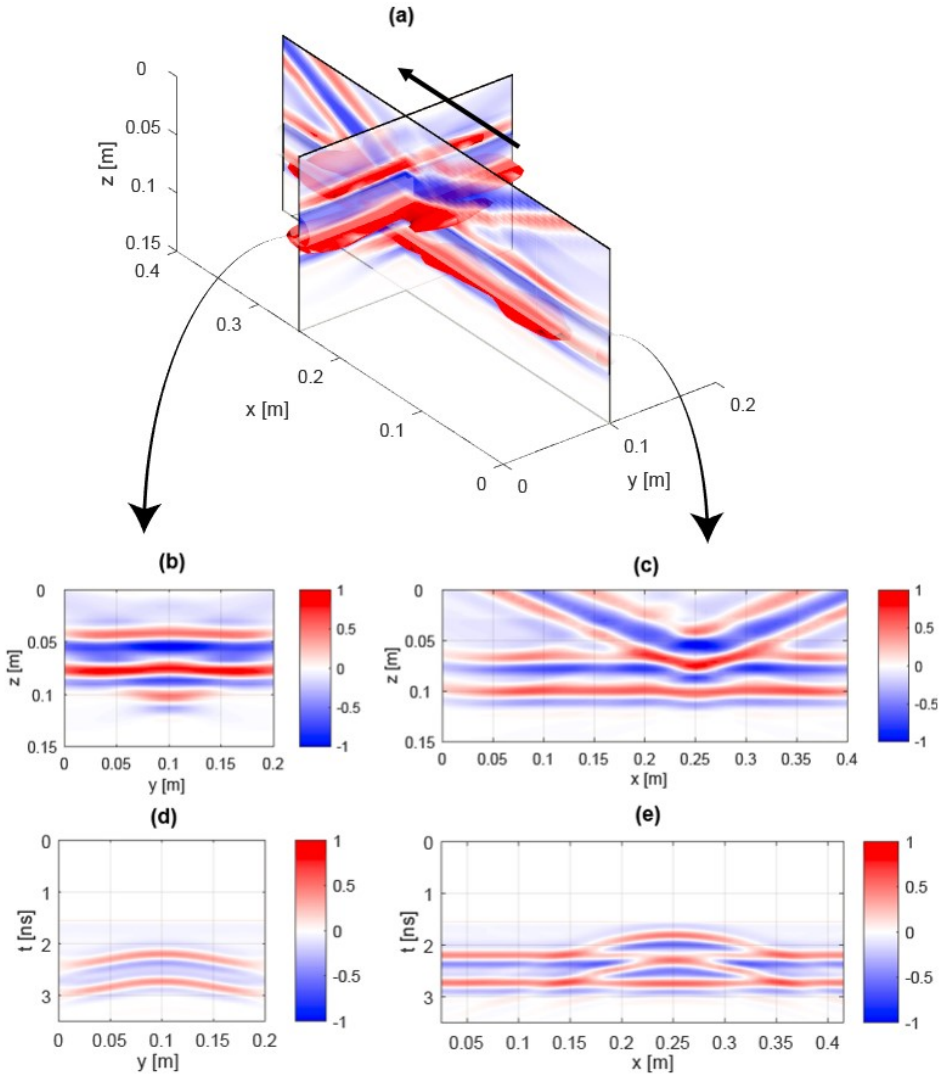


Figure 7: Resulting image of multistatic BPA applied on a synthetic multistatic air-coupled C-scan of a concrete slab with two crossing cylinders. (a) 3D view, arrow indicates GPR B-scan direction; (b) and (c) shows the indicated cross sections; (d) and (e) shows the corresponding raw data of the central receiver for each cross section.

## 4. CONCLUSIONS

In this work a fast 3D back-projection algorithm was introduced. The algorithm reduces the number of required computations by assuming that the refracted electromagnetic wave remains in the same plane as the incident wave. Under such assumption, simplifications for the estimation of the scattering point previously used in a two-dimensional case can be extended to the 3D domain. We presented a generalized form for the approximation of the scattering point and the back-projection method as simple, compact formulas. Furthermore, the BPA algorithm is suitable for parallelization, enabling the use of GPU that considerably reduces computation time with potential real-time application.

The BPA was applied to synthetic data. We show that the BPA can recover both object's shape and position with good accuracy on air-coupled bistatic and multistatic GPR systems. Complex arrangements such as the crossing cylinders can also be recovered using the BPA.

## ACKNOWLEDGEMENTS

This work is supported by the NSF Grants No. 1647095 and No. 1640687, the UVM SparkVT Fund, and VT EPSCoR.

## REFERENCES

[1] Daniels, J. D., [Ground Penetrating Radar, 2nd ed.], The Institution of Electrical Engineers, London, UK (2004).

[2] Huston, D., Xia, T., Zhang, Y., Fan, T., Orfeo, D. and Razinger, J., "Urban underground infrastructure mapping and assessment," 101680M (2017).

[3] Gamba, P. and Lossani, S., "Neural detection of pipe signatures in ground penetrating radar images," IEEE

Trans. Geosci. Remote Sens. **38**(2 I), 790–797 (2000).
[4] Xu, X., Xia, T., Venkatachalam, A. and Huston, D., "Development of High-Speed Ultrawideband Ground-Penetrating Radar for Rebar Detection," J. Eng. Mech. **139**(3), 272–285 (2013).
[5] Alani, A. M., Aboutalebi, M. and Kilic, G., "Applications of ground penetrating radar (GPR) in bridge deck monitoring and assessment," J. Appl. Geophys. **97**, 45–54 (2013).
[6] Wang, Z. W., Zhou, M., Slabaugh, G. G., Zhai, J. and Fang, T., "Automatic Detection of Bridge Deck Condition from Ground Penetrating Radar Images," IEEE Trans. Autom. Sci. Eng. **8**(3), 633–640 (2011).
[7] Al-Qadi, I. L., Xie, W., Roberts, R. and Leng, Z., "Data Analysis Techniques for GPR Used for Assessing Railroad Ballast in High Radio-Frequency Environment," J. Transp. Eng. **136**(4), 392–399 (2010).
[8] Jol, H. M., [Ground penetrating radar: theory and applications, 1sted.], Elsevier Science, Amsterdam, Netherlands (2009).
[9] Capineri, L., Grande, P. and Temple, J. A. G., "Advanced image-processing technique for real-time interpretation of ground-penetrating radar images," Int. J. Imaging Syst. Technol. **9**(1), 51–59 (1998).
[10] Ozdemir, C., Demirci, S., Enes, Y. and Kavak, A., "A Hyperbolic Summation Method to Focus B-Scan Ground Penetrating Radar Images: An Experimental Study With a Stepped Frequency System," Microw. Opt. Technol. **49**(3) (2007).
[11] Schneider, W. A., "Integral Formulation for Migration in Two and Three Dimensions," Geophysics **43**(1), 49–76 (1978).
[12] Gazdag, J., "Wave equation migration with the phase-shift method," Geophysics **43**(7), 1342–1351 (1978).
[13] Stolt, R. H., "Migration By Fourier Transform," Geophysics **43**(1), 23–48 (1978).
[14] Ozdemir, C., Demirci, S., Yigit, E. and Yilmaz, B., "A review on migration methods in b-scan ground penetrating radar imaging," Math. Probl. Eng. **2014** (2014).
[15] Chambers, D. and Paglieroni, D., "Real-Time Vehicle-Mounted Multistatic Ground Penetrating Radar Imaging System for Buried Object Detection," Lawrence Livermore Nat. Lab., Livermore, CA, USA, Tech. Rep. LLNL-TR-615452 (2013).
[16] Jung, H., Kang, W. and Kim, K., "Multilayer Stolt Migration Algorithm for Subsurface Target Imaging in Oblique Layers," 4295–4303 (2017).
[17] Herman, G. T., [Fundamentals of Computerized Tomography: Image Reconstruction from Projections, 2nded.], Springer-Verlag, London (2009).
[18] Herman, G. T., "Algorithms for Computed Tomography," Digit. Signal Process. Fundam., 26-1-26–10 (2010).
[19] Zhou, L., Huang, C. and Su, Y., "A fast back-projection algorithm based on cross correlation for GPR imaging," IEEE Geosci. Remote Sens. Lett. **9**(2), 228–232 (2012).
[20] Mast, J. E. and Johansson, E. M., [Three-dimensional ground-penetrating radar imaging using multifrequency diffraction tomography] (1994).
[21] Warren, C., Giannopoulos, A. and Giannakis, I., "gprMax: Open source software to simulate electromagnetic wave propagation for Ground Penetrating Radar," Comput. Phys. Commun. **209**, 163–170 (2016).
[22] Claerbout, J. F., "Imaging the Earth's Interior," Geophys. J. R. Astron. Soc. **86**(1), 217–217 (1986).
[23] Groves, P. D., [Principles of GNSS, inertial, and multisensor integrated navigation systems, 2nd edition [Book review], 2nded.], Artech House (2015).